Energies **2015**, *8*, 1848-1864; doi:10.3390/en8031848

OPEN ACCESS

energies

ISSN 1996-1073

www.mdpi.com/journal/energies

Article

A Linearized Large Signal Model of an LCL-Type Resonant Converter

Hong-Yu Li, Xiaodong Li *, Ming Lu and Song Hu

Faculty of Information Technology, Macau University of Science and Technology, Avenida Wai Long, Taipa, Macau SAR, China; E-Mails: lhy198984@126.com (H.-Y.L.); 1409853pii30001@student.must.edu.mo (M.L.); husong_2013@foxmail.com (S.H.)

* Author to whom correspondence should be addressed; E-Mail: xdli@must.edu.mo; Tel.: +853-8897-2195; Fax: +853-2882-3280.

Academic Editor: Frede Blaabjerg

Received: 10 January 2015 / Accepted: 27 February 2015 / Published: 5 March 2015

Abstract: In this work, an LCL-type resonant dc/dc converter with a capacitive output filter is modeled in two stages. In the first high-frequency ac stage, all ac signals are decomposed into two orthogonal vectors in a synchronous rotating *d*–*q* frame using multi-frequency modeling. In the dc stage, all dc quantities are represented by their average values with average state-space modeling. A nonlinear two-stage model is then created by means of a non-linear link. By aligning the transformer voltage on the *d*-axis, the nonlinear link can be eliminated, and the whole converter can be modeled by a single set of linear state-space equations. Furthermore, a feedback control scheme can be formed according to the steady-state solutions. Simulation and experimental results have proven that the resulted model is good for fast simulation and state variable estimation.

Keywords: resonant converter; multi-frequency modeling; soft-switching

1. Introduction

Resonant-type dc/dc converters with high-frequency (HF) isolation have been widely used in applications requiring high power density and high efficiency. Until now, many different topologies of resonant tanks have been discussed [1–7], such as the series LC-type, parallel LC-type, series-parallel LCC-type and LCL-type. Two different modulation methods, frequency modulation and phase-shift

modulation, are commonly used for the control of resonant dc/dc converters. With the frequency modulation, all switches are working with a fixed duty cycle and a variable switching frequency. A wide spectrum of harmonics naturally results. Meanwhile, a wide range of operating frequencies makes the design of frequency-sensitive components (passive filter, resonant tank, magnetic devices) difficult. The phase-shift modulation is featured with a fixed switching frequency and variable pulse-width. It is easy to implement and free of the main problems of frequency modulation mentioned before. Modeling a converter can reveal the interrelation among each parameter and give insight into the operation in the steady state and the dynamics. However, modeling of HF-isolated resonant-type dc/dc converters is difficult, because of a high number of reactive components and the non-linear switching behavior [8,9]. Small signal modeling is used to design a closed-loop controller for stable operation by investigating the system response to the small perturbation near a steady-state working point [10–13]. It can be based on the discrete time domain or the multiple frequency technique. Normally, discrete-time domain-based modeling is limited to a low order system. The multiple frequency method converts ac signals to dc signals at different frequencies and could generate a theoretically accurate model [14]. Although a small signal model is good for closed-loop design, it cannot provide a quick estimation of the converter state variables with large variation, especially when the converter has a larger operation range. By using the describing function, a nonlinear large signal model was proposed in [15], which resulted in non-linear controllers [16]. While nonlinear control is robust and accurate, it is complex and hard for practical implementation. In [17,18], a series-parallel LCC resonant converter with an inductive output filter is modeled with multiple frequency modeling and averaged state-space techniques. The obtained linearized large signal model can be linearized and results in a natural closed-loop control.

In this paper, an LCL resonant dc/dc converter with a capacitive output filter is selected to be modeled in this paper. The reason is that the LCL-type resonant tank is proven to be helpful for maintaining zero-voltage switching and high efficiency for a wide load range [19–24]. With a capacitive output filter, the voltage ringing on the diode rectifier due to an inductive output filter could be eliminated. To the best knowledge of the author, there is a lack in the literature of dedicated work for modeling the phase-shifted LCL resonant converter. The main features can be concluded as an aggregated linearized model for the phase-shift LCL resonant converter with a capacitive output filter constructed using fundamental harmonics approximation. Compared with previous works using the linear or nonlinear model, the obtained model could be used for fast estimation of the converter operation states without many complicated calculations involved. The obtained natural feedback control scheme is simple and straightforward and can be utilized for accurate closed-loop control if an additional simple controller (like a proportional-integral or proportional-integral-differential controller) is used.

The paper is organized as follows. In Section 2, The HF-isolated LCL resonant dc/dc converter is modeled in two stages according to different operating frequencies. A unified state-space model with a non-linear inner link is then created by combining two sub-models together. A natural linear feedback control is then obtained by aligning the transformer voltage with an axis in a synchronous rotating frame. Verification of the universal model and the feedback control is performed by MATLAB simulation and experimental testing on a laboratory converter prototype.

2. The LCL-Type Resonant dc/dc Converter with a Capacitive Output Filter

In Figure 1, the circuit diagram of an HF-isolated LCL-type resonant dc/dc converter is presented. Figure 2 illustrates its steady-state operation waveforms. The input dc voltage V_i is converted into an HF ac voltage v_{ab} by means of an HF full-bridge inverter. All switches are working with a fixed frequency. The two switches in each inverter leg are operated alternatively with a duty cycle slightly lower than 50%. There is a phase-shift between the two inverter legs, which is modulated to regulate the output voltage at different load level. Thus, the HF bridge inverter output voltage v_{ab} is a quasi-square wave. The series resonant frequency $\omega_r = 1/\sqrt{L_s C_s}$ defined by the LCL tank is normally designed to be quite close to the switching frequency ω_s. Therefore, the induced tank current i_s is nearly sinusoidal. The HF transformer voltage v_t is a square wave due to the assumption of a large capacitive output filter. The parallel inductor current i_p is a triangular waveform, which is helpful to extend the ZVS (zero-voltage switching) operation range as the load varies. The resulted transformer current i_t is rectified to a pulsing dc output current i_{dc} through the HF diode rectifier. The HF ac harmonics inside i_{dc} are then filtered out by the capacitive filter C_f. The leakage inductance of the transformer is included in the series resonant inductance L_s. The magnetic inductance of the transformer can be integrated with the parallel inductance L_p by proper magnetic design. The equivalent resistance r_s combines the winding resistance of the series inductor and the HF transformer, the on-state resistance of switches and diodes. r_f is the equivalent series resistance (ESR) of the filter capacitor.

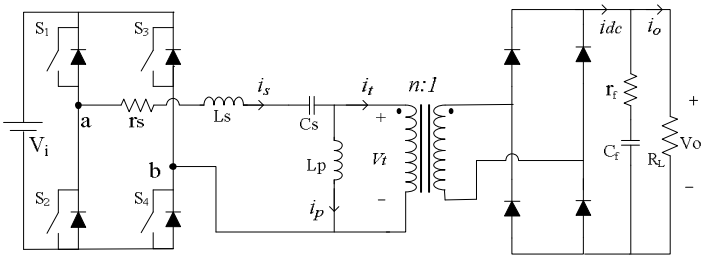

Figure 1. An LCL-type resonant dc/dc converter with a capacitive output converter.

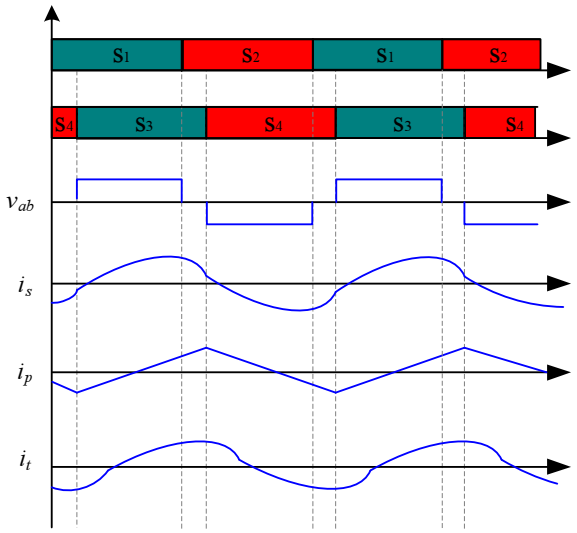

Figure 2. Steady-state operation waveforms of an LCL-type resonant converter.

3. A Nonlinear Model Based on a Two-Stage Equivalent Circuit

To perform the modeling of the LCL-type resonant converter, a simplified equivalent circuit of the LCL-type converter with the active switch network and the HF transformer removed is illustrated in Figure 3. All quantities have been reflected on the primary side, and the reflected secondary parameters are marked with a superscript " ′ ". The snubber effect and switching transients are neglected.

As a multi-stage conversion system, this converter can be divided into two sub-systems with the HF diode bridge as the boundary: the HF ac sub-system and the dc sub-system. In the following analysis, mathematical models will be constructed for each sub-system and then linked together according to the nature of the diode rectifier.

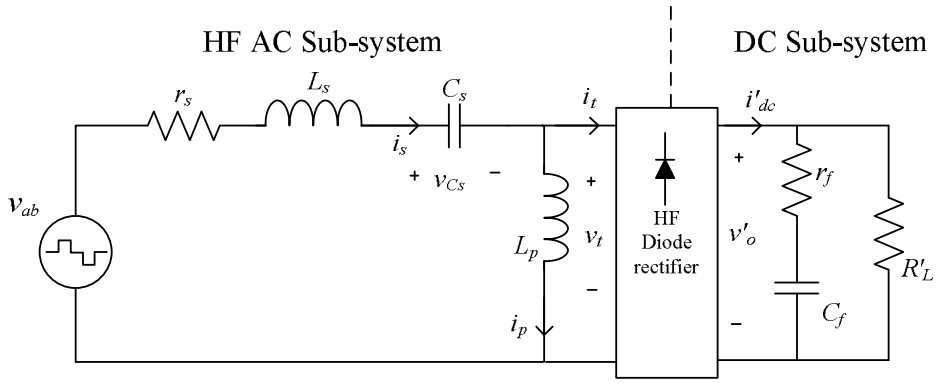

Figure 3. A two-stage equivalent circuit.

3.1. Modeling of the HF AC Sub-System Using Phasor Transformation

As seen from Figure 4, the HF ac sub-system consists of two voltage sources and an impedance network. The right-side voltage source v_{t} is the primary-side voltage of the HF transformer (also the voltage across the parallel inductor L_{p}), which stems from the ripple-free output voltage via the operation of the HF diode bridge. The set of differential equations describing the dynamics of the three reactive components can be written as:

$$v_{\mathrm{ab}} = i_{\mathrm{s}} r_{\mathrm{s}} + L_{\mathrm{s}} \frac{di_{\mathrm{s}}}{dt} + v_{\mathrm{Cs}} + v_{\mathrm{t}} \tag{1}$$

$$i_{\mathrm{s}} = C_{\mathrm{s}} \frac{dv_{\mathrm{Cs}}}{dt} \tag{2}$$

$$v_{\mathrm{t}} = L_{\mathrm{p}} \frac{di_{\mathrm{p}}}{dt} \tag{3}$$

The transformer current is obtained as:

$$i_{\mathrm{t}} = i_{\mathrm{s}} - i_{\mathrm{p}} \tag{4}$$

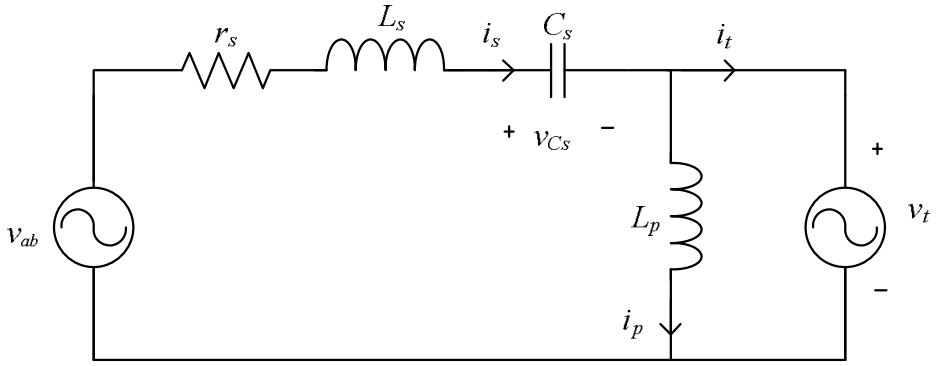

Figure 4. Equivalent circuit of the high-frequency (HF) ac sub-system.

As mentioned before, the inductor current i_{s} and capacitor voltage v_{Cs} are nearly sinusoidal due to the close-to-resonance operation. Additionally, the HF inverter output voltage v_{ab}, the transformer voltage v_{t}, the parallel inductor current i_{p} and the transformer current i_{t} are all ac-dominant signals. Therefore, it is reasonable to use only the fundamental components to approximate each ac voltage and current in this converter. To explore the dynamics of the HF sub-system, the set of state equations are converted into the phasor domain firstly:

$$\mathbf{v}_{\mathrm{ab}} = \mathbf{i}_{\mathrm{s}} r_{\mathrm{s}} + L_{\mathrm{s}}\left(\frac{d\mathbf{i}_{\mathrm{s}}}{dt} + j\omega_{\mathrm{s}}\mathbf{i}_{\mathrm{s}}\right) + \mathbf{v}_{\mathrm{Cs}} + \mathbf{v}_{\mathrm{t}} \tag{5}$$

$$\mathbf{i}_{\mathrm{s}} = C_{\mathrm{s}}\left(\frac{d\mathbf{v}_{\mathrm{Cs}}}{dt} + j\omega_{\mathrm{s}}\mathbf{v}_{\mathrm{Cs}}\right) \tag{6}$$

$$\mathbf{v}_{\mathrm{t}} = L_{\mathrm{p}}\left(\frac{d\mathbf{i}_{\mathrm{p}}}{dt} + j\omega_{\mathrm{s}}\mathbf{i}_{\mathrm{p}}\right) \tag{7}$$

$$\mathbf{i}_{\mathrm{t}} = \mathbf{i}_{\mathrm{s}} - \mathbf{i}_{\mathrm{p}} \tag{8}$$

For each sinusoidal voltage or current, its corresponding phasor can be expressed in a *d*–*q* coordination system rotating with an angular speed ω_{s}. For example:

$$v(t) = V_{\mathrm{m}}\cos(\omega_{\mathrm{s}}t + \phi) = \Re[\mathbf{V}e^{j\omega_{\mathrm{s}}t}] = \Re[(v_{\mathrm{d}} + jv_{\mathrm{q}})e^{j\omega_{\mathrm{s}}t}] \tag{9}$$

The *d*-axis and *q*-axis values are orthogonal functions of the time t and would be constants in the steady state. The components along the d-axis and q-axis can be evaluated as:

$$v_{\mathrm{d}} = \frac{2}{T}\int_{\mathrm{t\text{-}T}}^{T} v(\tau)\cos\omega_{\mathrm{s}}\tau d\tau \tag{10}$$

$$v_{\mathrm{q}} = \frac{2}{T}\int_{\mathrm{t\text{-}T}}^{T} v(\tau)\sin\omega_{\mathrm{s}}\tau d\tau \tag{11}$$

By using such a phasor transformation, all ac signals in Equations (5)–(8) can be written as phasors in the d–q rotating frame:

$$\mathbf{i}_{\mathrm{s}} = i_{\mathrm{sd}} + j i_{\mathrm{sq}} \quad (12)$$

$$\mathbf{v}_{\mathrm{Cs}} = v_{\mathrm{Csd}} + j v_{\mathrm{Csq}} \quad (13)$$

$$\mathbf{i}_{\mathrm{p}} = i_{\mathrm{pd}} + j i_{\mathrm{pq}} \quad (14)$$

$$\mathbf{v}_{\mathrm{ab}} = v_{\mathrm{abd}} + j v_{\mathrm{abq}} \quad (15)$$

$$\mathbf{v}_{\mathrm{t}} = v_{\mathrm{td}} + j v_{\mathrm{tq}} \quad (16)$$

$$\mathbf{i}_{\mathrm{t}} = i_{\mathrm{td}} + j i_{\mathrm{tq}} \quad (17)$$

Thus, Equations (5)–(8) can be decoupled along the d-axis and q-axis, respectively, by using Equations (12)–(17).

$$v_{\mathrm{abd}} = i_{\mathrm{sd}} r_{\mathrm{s}} + L_{\mathrm{s}}\left(\frac{di_{\mathrm{sd}}}{dt} - \omega_{\mathrm{s}} i_{\mathrm{sq}}\right) + v_{\mathrm{Csd}} + v_{\mathrm{td}} \quad (18)$$

$$v_{\mathrm{abq}} = i_{\mathrm{sq}} r_{\mathrm{s}} + L_{\mathrm{s}}\left(\frac{di_{\mathrm{sq}}}{dt} + \omega_{\mathrm{s}} i_{\mathrm{sd}}\right) + v_{\mathrm{Csq}} + v_{\mathrm{tq}} \quad (19)$$

$$i_{\mathrm{sd}} = C_{\mathrm{s}}\left(\frac{dv_{\mathrm{Csd}}}{dt} - \omega_{\mathrm{s}} v_{\mathrm{Csq}}\right) \quad (20)$$

$$i_{\mathrm{sq}} = C_{\mathrm{s}}\left(\frac{dv_{\mathrm{Csq}}}{dt} + \omega_{\mathrm{s}} v_{\mathrm{Csd}}\right) \quad (21)$$

$$v_{\mathrm{td}} = L_{\mathrm{p}}\left(\frac{di_{\mathrm{pd}}}{dt} - \omega_{\mathrm{s}} i_{\mathrm{pq}}\right) \quad (22)$$

$$v_{\mathrm{tq}} = L_{\mathrm{p}}\left(\frac{di_{\mathrm{pq}}}{dt} + \omega_{\mathrm{s}} i_{\mathrm{pd}}\right) \quad (23)$$

$$i_{\mathrm{td}} = i_{\mathrm{sd}} - i_{\mathrm{pd}} \quad (24)$$

$$i_{\mathrm{tq}} = i_{\mathrm{sq}} - i_{\mathrm{pq}} \quad (25)$$

Equations (18)–(25) can be reorganized into the standard form of the state-space equations:

$$\dot{\vec{x}}_1(t) = A_1 \vec{x}_1(t) + B_1 \vec{u}_1(t) \quad (26)$$

$$\vec{y}_1(t) = C_1 \vec{x}_1(t) + D_1 \vec{u}_1(t) \quad (27)$$

where the state-space variables vector $\vec{x}_1(t)$, the input vector $\vec{u}_1(t)$ and the output vector $\vec{y}_1(t)$ are defined as:

$$\vec{x}_1(t) = [i_{\mathrm{sd}} \;\; i_{\mathrm{sq}} \;\; v_{\mathrm{Csd}} \;\; v_{\mathrm{Csq}} \;\; i_{\mathrm{pd}} \;\; i_{\mathrm{pq}}]^T \quad (28)$$

$$\vec{u}_1(t) = [v_{\mathrm{abd}} \;\; v_{\mathrm{abq}} \;\; v_{\mathrm{td}} \;\; v_{\mathrm{tq}}]^T \quad (29)$$

$$\vec{y}_1(t) = [i_{\mathrm{td}} \;\; i_{\mathrm{tq}}]^T \quad (30)$$

and the four coefficient matrices A_1, B_1, C_1, D_1 are defined as:

$$A_1 = \begin{bmatrix} -\frac{r_s}{L_s} & \omega_s & -\frac{1}{L_s} & 0 & 0 & 0 \\ -\omega_s & -\frac{r_s}{L_s} & 0 & -\frac{1}{L_s} & 0 & 0 \\ \frac{1}{C_s} & 0 & 0 & \omega_s & 0 & 0 \\ 0 & \frac{1}{C_s} & -\omega_s & 0 & 0 & 0 \\ 0 & 0 & 0 & 0 & 0 & \omega_s \\ 0 & 0 & 0 & 0 & -\omega_s & 0 \end{bmatrix} \quad (31)$$

$$B_1 = \begin{bmatrix} \frac{1}{L_s} & 0 & -\frac{1}{L_s} & 0 \\ 0 & \frac{1}{L_s} & 0 & -\frac{1}{L_s} \\ 0 & 0 & 0 & 0 \\ 0 & 0 & 0 & 0 \\ 0 & 0 & \frac{1}{L_p} & 0 \\ 0 & 0 & 0 & \frac{1}{L_p} \end{bmatrix} \quad (32)$$

$$C_1 = \begin{bmatrix} 1 & 0 & 0 & 0 & -1 & 0 \\ 0 & 1 & 0 & 0 & 0 & -1 \end{bmatrix} \quad (33)$$

$$D_1 = [0 \ 0 \ 0 \ 0] \quad (34)$$

3.2. Modeling of the DCSub-System

The equivalent circuit of the dc sub-system is presented in Figure 5. All voltages and currents in this subsystem are dc dominant and are represented by their average values only. The left current source $\bar{i}'_{dc}$ is the average output current of the diode rectifier, and the right one is the average load current $\bar{i}'_o$. $\bar{v}'_o$ is the average output voltage. $\bar{v}'_{Cf}$ is the average filter capacitor voltage. The differential equations describing the dc sub-system are concluded as:

$$\bar{i}'_{dc} = C_f \frac{d\bar{v}'_{Cf}}{dt} + \bar{i}'_o \quad (35)$$

$$\bar{v}'_o = \bar{v}'_{Cf} + r_f(\bar{i}'_{dc} - \bar{i}'_o) \quad (36)$$

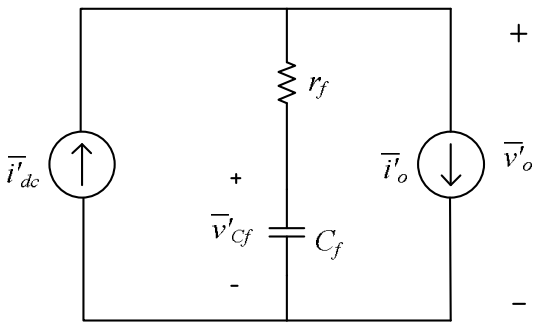

Figure 5. Equivalent circuit of the dc sub-system.

Following a similar principle as in the last section, the state variable vector $\vec{x}_2(t)$, the input vector $\vec{u}_2(t)$ and the output vector $\vec{y}_2(t)$ for the dc sub-system can be defined as:

$$\vec{x}_2(t) = [\bar{v}'_{\mathrm{Cf}}] \tag{37}$$
$$\vec{u}_2(t) = [\bar{i}'_{\mathrm{dc}} \ \ \bar{i}'_{\mathrm{o}}]^T \tag{38}$$
$$\vec{y}_2(t) = [\bar{v}'_{\mathrm{o}}] \tag{39}$$

Thus, the standard state-space model of the dc sub-system looks like:

$$\dot{\vec{x}}_2(t) = A_2\vec{x}_2(t) + B_2\vec{u}_2(t) \tag{40}$$
$$\vec{y}_2(t) = C_2\vec{x}_2(t) + D_2\vec{u}_2(t) \tag{41}$$

where the resulting coefficients matrices A_2, B_2, C_2, D_2 are:

$$A_2 = [0]\,; \quad B_2 = \begin{bmatrix} \frac{1}{C_{\mathrm{f}}} & -\frac{1}{C_{\mathrm{f}}} \end{bmatrix}; \quad C_2 = [1]\,; \quad D_2 = \begin{bmatrix} \frac{1}{r_{\mathrm{f}}} & -\frac{1}{r_{\mathrm{f}}} \end{bmatrix} \tag{42}$$

3.3. Modeling of the Diode Bridge Rectifier

According to the waveforms in Figure 2, the function of the diode rectifier is to convert the sinusoidal i_{t} into a pulsing dc current and to convert the square-wave v_{t} into a nearly ripple-free $\bar{v}'_{\mathrm{o}}$. If only average values of the dc-dominant signals are considered in the dc sub-system, the relationship across the diode bridge can be concluded as follows: the current source $\bar{i}'_{\mathrm{dc}}$ (one of the inputs of the dc sub-system) is the average of the rectified current i_{t} (the output of the ac sub-system), and the output voltage $\bar{v}'_{\mathrm{o}}$ is the average of the rectified fundamental transformer voltage v_{t}:

$$\bar{i}'_{\mathrm{dc}} = \frac{2}{\pi} i_{\mathrm{t,peak}} = \frac{2}{\pi}\sqrt{i_{\mathrm{td}}^2 + i_{\mathrm{tq}}^2} \tag{43}$$
$$\bar{v}'_{\mathrm{o}} = \frac{\pi}{4} v_{\mathrm{t,peak}} = \frac{\pi}{4}\sqrt{v_{\mathrm{td}}^2 + v_{\mathrm{tq}}^2} \tag{44}$$

With the assumption of a lossless power transfer, the power on both sides of the diode bridge should be balanced as:

$$\bar{v}'_{\mathrm{o}} \cdot \bar{i}'_{\mathrm{dc}} = \frac{1}{2}(i_{\mathrm{td}} v_{\mathrm{td}} + i_{\mathrm{tq}} v_{\mathrm{tq}}) \tag{45}$$

By means of Equations (43)–(45), the two models in each stage can be linked together now as shown in Figure 6. Due to the existence of the square root operation in Equation (43), the combined model of the LCL-type resonant converter is nonlinear.

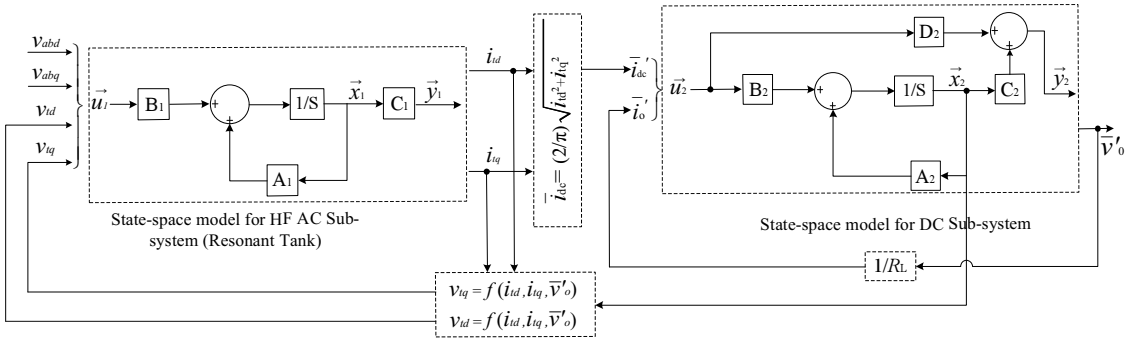

Figure 6. A nonlinear model of LCL-type resonant dc/dc converter.

3.4. Steady-State Solutions of the Nonlinear Model

The steady-state solutions of all state variables could be found by simply setting the derivative vectors of state variables in Equations (26), (27), (40) and (41) to be zero.

The steady-state solutions of the HF ac sub-system are given as:

$$\vec{X}_1 = -A_1^{-1} \cdot B_1 \cdot \vec{U}_1 \tag{46}$$

where $\vec{X}_1$ and $\vec{U}_1$ are steady-state values of $\vec{x}_1$ and $\vec{u}_1$, respectively:

$$\vec{X}_1 = [I_{\text{sd}} \;\; I_{\text{sq}} \;\; V_{\text{Csd}} \;\; V_{\text{Csq}} \;\; I_{\text{pd}} \;\; I_{\text{pq}}]^T; \tag{47}$$

$$\vec{U}_1 = [V_{\text{abd}} \;\; V_{\text{abq}} \;\; V_{\text{td}} \;\; V_{\text{tq}}]^T \tag{48}$$

Based on Equation (46), the input voltage V_{ab} should satisfy the following conditions to get the particular I_{t} and V_{t} in the steady state:

$$V_{\text{abd}} = m_1 I_{\text{td}} + m_2 I_{\text{tq}} + m_3 V_{\text{td}} + m_4 V_{\text{tq}} \tag{49}$$

$$V_{\text{abq}} = m_1 I_{\text{tq}} - m_2 I_{\text{td}} + m_3 V_{\text{tq}} - m_4 V_{\text{td}} \tag{50}$$

where:

$$m_1 = r_{\text{s}}; \quad m_2 = \frac{1}{\omega_{\text{s}} C_{\text{s}}} - \omega_{\text{s}} L_{\text{s}}; \quad m_3 = 1 - \frac{m_2}{\omega_{\text{s}} L_{\text{p}}}; \quad m_4 = \frac{m_1}{\omega_{\text{s}} L_{\text{p}}}$$

The steady-state solutions of the dc sub-system are given as:

$$\bar{I}'_{\text{dc}} = \bar{I}'_{\text{o}} \quad \bar{V}'_{\text{o}} = \bar{V}'_{\text{Cf}} \tag{51}$$

The relationship described in Equations (43)–(45) is still valid for those steady-state values and can be combined with Equations (49)–(51) to find any particular parameter.

4. A Linearized Model of the LCL-Type Resonant Converter

Equations (49) and (50) reveal that the required components of V_{ab} along the d-axis or q-axis are decided by both the d-axis component and q-axis component of V_{t} and I_{t}. In order to decouple the d–q interconnection, v_{t} is assumed to be on the d-axis, *i.e.*, $v_{\text{t}} = v_{\text{td}}$, $v_{\text{tq}} = 0$. With this assumption, the following results can be gotten from Equations (43)–(45):

$$i_{\text{tq}} = 0; \quad i_{\text{td}} = \frac{\pi}{2} \bar{i}'_{\text{dc}}; \quad v_{\text{td}} = \frac{4}{\pi} \bar{v}'_{\text{o}} \tag{52}$$

which indicates that both i_{t} and v_{t} have only the d-axis component, and thus, they are always in phase. This consequence is actually valid, because v_{t} and i_{t} are the input voltage and input current of the HF diode rectifier. Furthermore, the nonlinear calculation, including the square root, in Equations (43)–(45) is eliminated now. According to the linearization (v_{t} and i_{t} containing only d-axis values), Equations (49)–(50) are reduced to:

$$V_{\text{abd}} = m_1 I_{\text{td}} + m_3 V_{\text{td}} \tag{53}$$

$$V_{\text{abq}} = -m_2 I_{\text{td}} - m_4 V_{\text{td}} \tag{54}$$

It can be seen that in the steady state, the d–q components of V_{ab} are decided by I_{td} and V_{td} only, which, in turn, are proportional to the load current and the load voltage, respectively. If the equivalent parasitic resistance r_{s} is neglected, Equations (56)–(57) can be reduced further into:

$$V_{\text{abd}} = m_3 V_{\text{td}}; \quad V_{\text{abq}} = -m_2 I_{\text{td}} \tag{55}$$

It is seen that the control of the output voltage and the output current are decoupled, and they are decided by V_{abq} and V_{abq}, respectively.

Equations (53) and (54) are also actually the necessary conditions to meet the requirement for linearization of the relationship between two sub-systems, *i.e.*, only such an input voltage V_{ab} can result in $I_{\text{t}} = I_{\text{td}}; \quad V_{\text{t}} = V_{\text{td}}$. Therefore, a natural feedback scheme can be formed in the dynamics. The actual controllable input voltage v_{ab} could be decided by:

$$v_{\text{abd}} = m_1 i_{\text{cm}} + m_3 v_{\text{td}} \tag{56}$$

$$v_{\text{abq}} = -m_2 i_{\text{cm}} - m_4 v_{\text{td}} \tag{57}$$

where i_{cm} in each equation is the current command, which indicates the level of converter output current.

The term including v_{td} in each equation is the weighted state feedback for linearization. The obtained linearized model of the LCL-type resonant converter is given in Figure 7. In this feedback control scheme, the only parameter needed to be sampled is the output voltage.

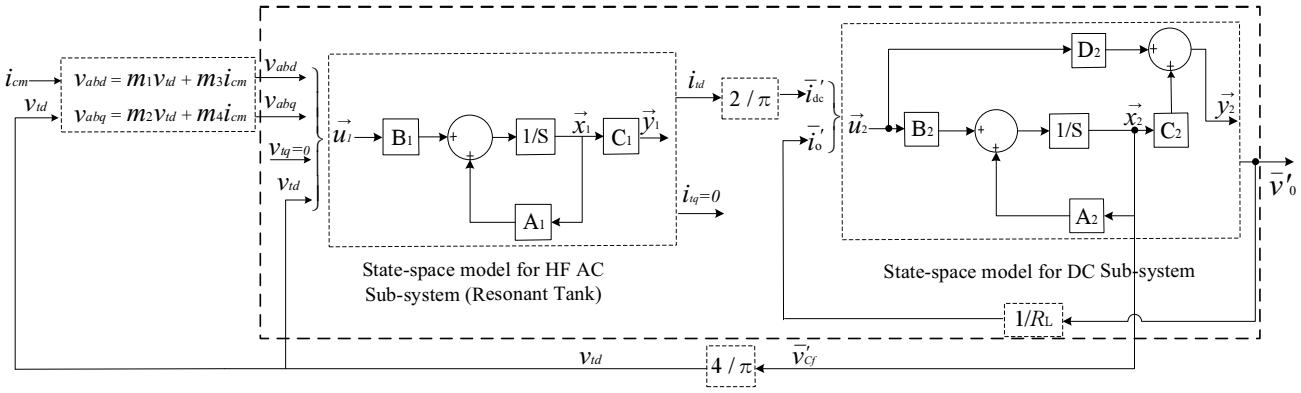

Figure 7. A linearized model of an LCL-type resonant dc/dc converter with feedback control.

Additionally, the two sub-systems can be described using only one set of state-space equations.

$$\dot{\vec{x}}(t) = A\vec{x}(t) + B\vec{u}(t); \quad \vec{y}(t) = C\vec{x}(t) + D\vec{u}(t) \tag{58}$$

The new state variables vector $x(t)$, input vector $u(t)$ and output vector $y(t)$ are defined as:

$$\vec{x}(t) = [i_{\text{sd}} \ i_{sq} \ v_{\text{Csd}} \ v_{\text{Csq}} \ i_{\text{pd}} \ i_{\text{pq}} \ v'_{\text{Cf}}]^T; \tag{59}$$

$$\vec{u}(t) = [i_{\text{cm}} \ i'_{\text{o}}]^T; \tag{60}$$

$$\vec{y}(t) = [v'_{\text{o}}] \tag{61}$$

and the four new coefficients matrices are defined as:

$$A = \begin{bmatrix} -\frac{r_s}{L_s} & \omega_s & -\frac{1}{L_s} & 0 & 0 & 0 & \frac{4(m_3-1)}{\pi L_s} \\ -\omega_s & -\frac{r_s}{L_s} & 0 & -\frac{1}{L_s} & 0 & 0 & \frac{-4m_4}{\pi L_s} \\ \frac{1}{C_s} & 0 & 0 & \omega_s & 0 & 0 & 0 \\ 0 & \frac{1}{C_s} & -\omega_s & 0 & 0 & 0 & 0 \\ 0 & 0 & 0 & 0 & 0 & \omega_s & \frac{4}{\pi L_p} \\ 0 & 0 & 0 & 0 & -\omega_s & 0 & 0 \\ 0 & 0 & 0 & 0 & 0 & 0 & 0 \end{bmatrix}$$

$$B = \begin{bmatrix} \frac{m_1}{L_s} & -\frac{m_2}{L_s} & 0 & 0 & 0 & 0 & \frac{2}{\pi C_f} \\ 0 & 0 & 0 & 0 & 0 & 0 & -\frac{1}{C_f} \end{bmatrix}^T$$

$$C = \begin{bmatrix} 0 & 0 & 0 & 0 & 0 & 0 & 1 \end{bmatrix}$$

$$D = \begin{bmatrix} \frac{1}{r_f} & -\frac{1}{r_f} \end{bmatrix}$$

5. Validation through Simulation and Experimental Results

In order to evaluate the accuracy of the developed model, the simulation and experimental results are presented in this section. In Table 1, the specifications of the converter to be investigated are presented. The design of the converter is based on the steady-state analysis using the Fourier series approach presented in [19]. For the selection of the design parameters and design procedures, the reader can refer to [19], too.

Table 1. Converter specifications for illustration. ESR, equivalent series resistance.

Input dc voltage	60 V	Output dc voltage	48 V
Rated power	100 W	Switching frequency	100 kHz
Series inductance L_s	26 μH	Series capacitance C_s	118 nF
Parallel inductance L_p	260 μH	Turns ratio of the transformer	12:10
Output filter C_f	200 μF	ESR of C_f	0.3 Ω
Equivalent resistance r_s	0.2 Ω		

At first, simulation on the combined model in Equation (58) is performed in MATLAB/Simulink. The converter starts with the half load (the control input i_{cm} = 1.357 A and load resistance $R_L = 46.08\ \Omega$ at $t = 0$ s). The transient response is then investigated by changing the load level from half load to full load ($i_{ct} = 2.713\ A,\ R_L = 23.04\ \Omega$) at $t = 0.5$ s. The resulting plots are presented Figure 8. It is observed that i_{td} and i_{sd} are exactly the same, and they follow the change of the current command i_{cm}. In the steady state, v_{Csq}, v_{Csd} are proportional to i_{sd}, i_{sq}, respectively. As predicted, i_{tq} and i_{pd} are nearly zero, except for the transient of load-changing. i_{sq} is equal to i_{pq} in the steady state when the i_{tq} settles down to zero. The transformer voltage v_{td} and output voltage v'_o remain almost unchanged during the transient of load-changing.

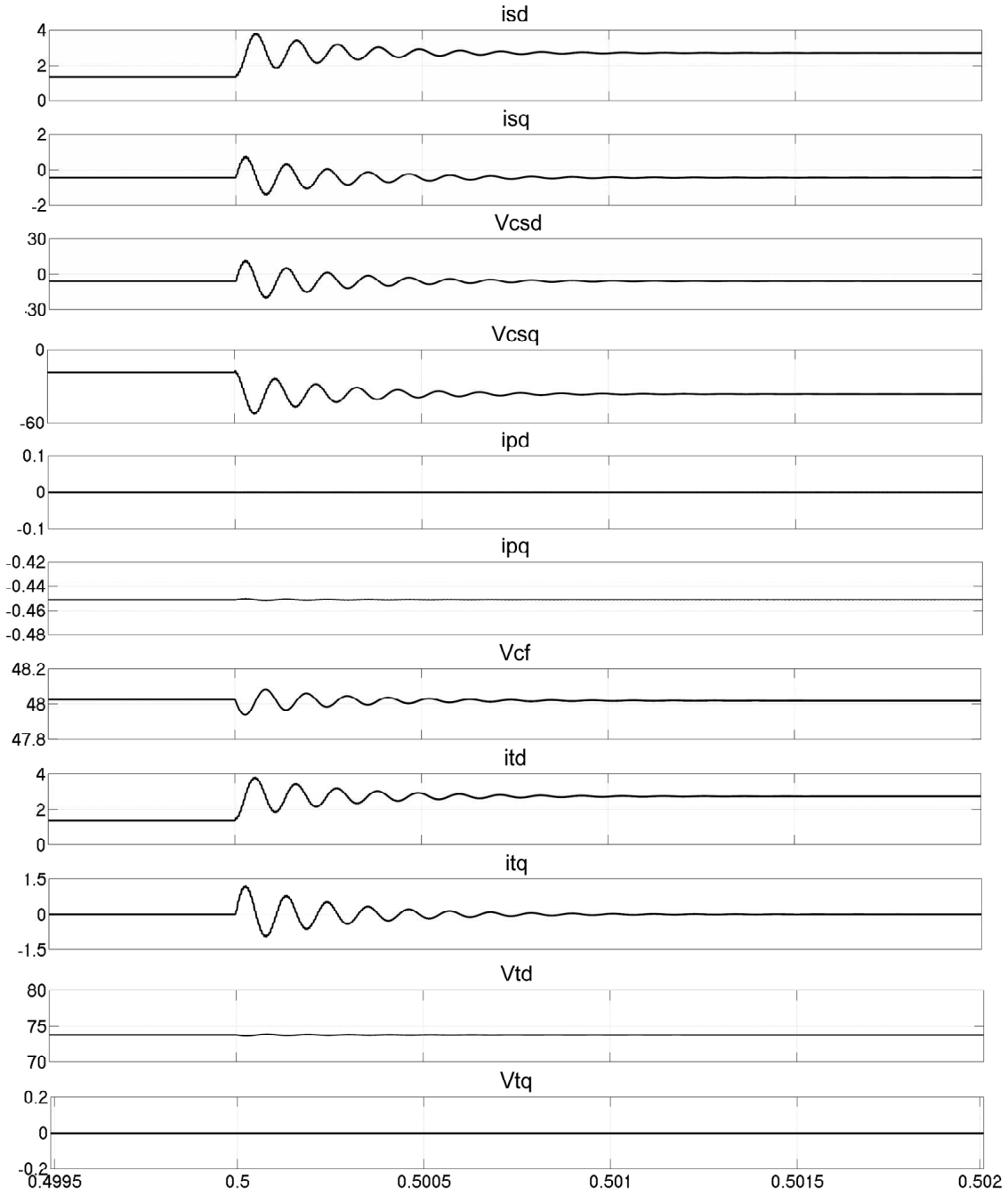

Figure 8. Simulation results from MATLAB/Simulink. From top to bottom: i_{sd}, i_{sq}, v_{Csd}, v_{Csq}, i_{pd}, i_{pq}, v_{Cf}, i_{td}, i_{tq}, v_{td}, v_{tq}.

A lab prototype of the LCL converter with the same specifications was built and tested, too. One pair of ETD39 cores (material N97, EPCOS AG, Munich, Germany) is used as the core of the HF transformer. The windings are made of multi-thread litz wire with a turn ratio of 12:11. Both the series inductor and the parallel inductor are built with a toroidal core (material Ni–Fe permalloy). The main switches used in the full bridge are HEXFET® power MOSFET IRFR4620 (International Rectifier, El Segundo, CA, USA). Additionally, the power diodes used in the HF rectifier are MUR1560 with ultrafast recovery time. To take the leakage and magnetic inductance of the HF transformer, the parallel inductor L_{p} is put on the secondary side of the HF transformer. The calculation of the feedback control and the generation of

gating signals are implemented in an Altera Cyclone II FPGA development board. As the main switch has a low switching delay, the deadband of gating signals is selected at 150 ns.

It should be noted that the control scheme is not a proper closed-loop control, even though a natural feedback control exists. Normally, most of the load is the constant-voltage type, so that it is the converter output voltage rather than the output current that should be kept constant when the load resistance changes. However, the control input in this feedback control scheme is the output current, which means that in order to keep output voltage constant, the current command should be adjusted instantly whenever a change of load resistance happens. Thus, in practical applications, the current command should be determined by means of an extra feedback output voltage or current controller, whose design deserves more work in the future. For the actual test reported in this paper, a constant voltage-type load is used instead of a resistive load to evaluate the accuracy of the natural feedback control scheme only.

The steady-state experimental waveforms with open-loop control are presented in Figure 9 for full load and half load operation. v_{AB} is a quasi-square wave voltage with a different pulse width when the load level varies. v_{t} is a full square-wave voltage at full load. However, it has a ringing part at partial load, in which the secondary current is almost zero, and there is a resonance between the three resonant tank components. In spite of this irregularity, it can be seen that v_{t} and i_{t} are still in phase, which indicates the correctness of the previous assumption made in Section 4.

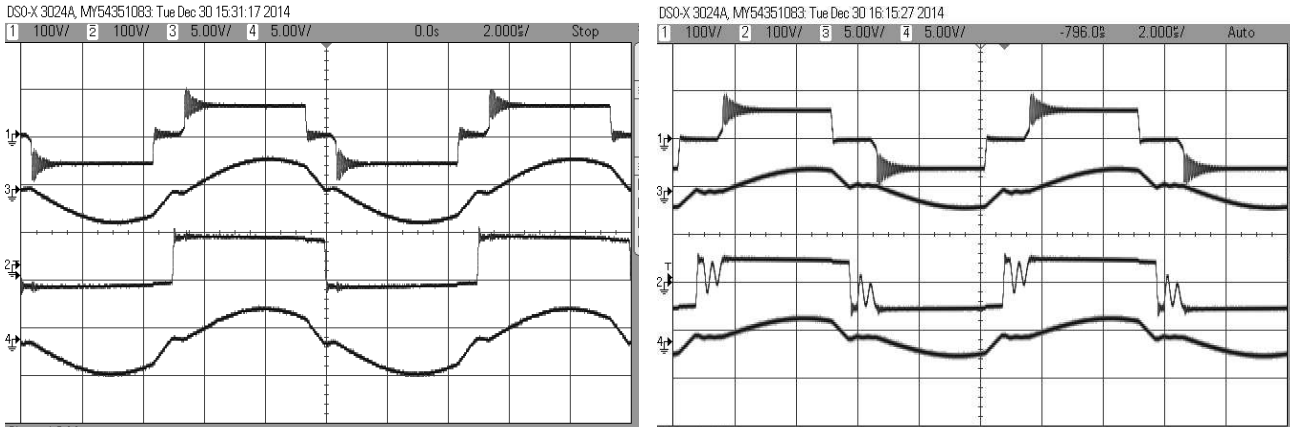

(**a**) (**b**)

Figure 9. Experimental plots of: (**a**) output power, 100 W; (**b**) output power, 50 W. Waveforms from top to bottom in each case: v_{AB}, i_{s}, v_{t} (on the secondary side), i_{t} (on the secondary side). Voltage scale: 100 V/div; current scale: 5 A/div.

In Table 2, a comparison is also made for RMS (root-mean-square) values of important state variables in the steady state between the simulation results and experimental test. A certain degree of match for most of parameters can be found from Table 2. The difference originates from two parts: the non-ideal components in the experiment and the approximation analysis approach using fundamental sinusoidal signals only. Generally, the deviations in partial load are higher than those in the full load condition. The reason is that there are more high-order harmonics in each quantity under the partial load condition. Furthermore, the deviation of v_t is much higher than the others, because v_t is a square-wave signal, while the others assemble sinusoidal signals.

Table 2. Comparison of key parameters between experimental results and the proposed model.

	P_o = 100 W		P_o = 50 W	
	Model	**Experiment**	**Model**	**Experiment**
$i_{s,rms}$ (A)	1.945	2.22	1.018	1.298
$i_{t,rms}$ (A)	2.315	2.488	1.157	1.283
$v_{t,rms}$ (A)	43.24	51.26	43.23	50.96
$v_{Cs,rms}$ (V)	26.238	29.35	13.635	15.936

Then, the closed-loop control with the natural feedback scheme is tested by a similar transient test as in the simulation. The four curves shown in Figure 10 are the series resonant current i_s, the resonant capacitor voltage v_{Cs}, the transformer voltage v_t and current i_t measured from the secondary side. With the change of current command, the indicators of the load level (i_t) and resonant tank parameters (i_s, v_{Cs}) rose from half load operation to full load operation. The settling time is approximately 1.5 ms, which is longer than the simulation results. The power level control is not accurate, with 7% and 11% at full load and half load conditions, respectively. The reason can be be attributed to: (1) the approximation used in the modeling procedure; (2) the error in measurement and estimation of the parameters used in the calculation (like L_s, C_s, r_f, r_s); (3) other non-ideal conditions in the real test (like the effect of the deadband of gating signals, *etc.*). To eliminate the apparent steady-state error, an extra compensation controller is needed to generate accurate gating signals. Since the natural feedback scheme itself is linear, a low-order PI or PID controller might be sufficient for better performance.

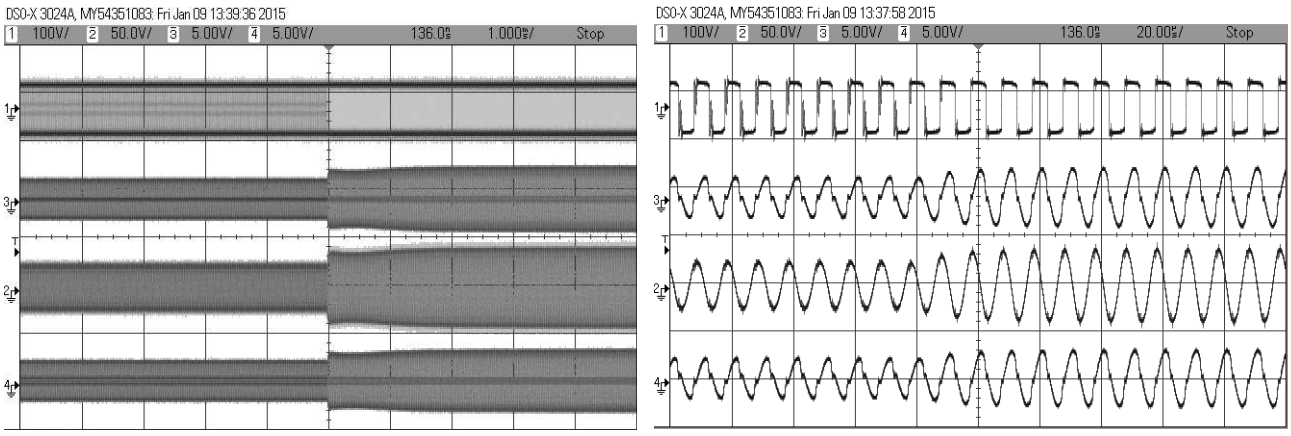

(**a**) (**b**)

Figure 10. Experimental plots of the transient condition from half load to full load: (**a**) time scale, 1 ms/div; (**b**) expended view at time scale 20 µs/div. Waveforms from top to bottom in each case: v_t (100 V/div) (on the secondary side), i_s (5 A/div), v_{Cs} (50 V/div), i_t (5 A/div) (on the secondary side).

6. Conclusions

In this paper, the proposed work addressed the modeling of an HF-isolated LLC resonant converter with a capacitive output filter. The modeling technique combines the simple sinusoidal approximation

in a synchronous rotating frame with the conventional dc state-space averaging approach. Based on the main operating frequency in two different conversion stages in the converter, two state-space models for high-frequency ac and dc are derived and linked with a non-linear relationship. Then, by aligning the synchronous rotating reference frame for the HF ac stage with one component of the transformer voltage, the inter-stage link is linearized, so that both HF ac and dc variables can be combined together to generate a unified state-space model. A weighted state feedback scheme is naturally obtained according to the steady-state solutions. Both simulation plots and experimental results show that the developed linear aggregated model can be used to estimate the operation condition of the converter with easy calculation and an acceptable accuracy level. Although the natural state feedback control is not quite accurate for power regulation due to the approximation in the analysis, it lays a good base for further precise closed-loop control, since no additional compensation controllers are used now. In future work, further efforts are needed to design extra voltage/current controllers to compensate for the errors introduced in the theoretical calculation and to improve the stability.

Acknowledgments

The authors would like to thank the financial support from the Science and Technology Development Fund of Macau (FDCT) under Grant Agreement No. 067/2011/A.

Author Contributions

Mr. Hong-Yu Li was responsible for the theoretical derivation and proving and for paper writing. The main contribution of Xiaodong Li was the planing, coordination and consultation of the whole project. Mr. Ming Lu made a contribution to the circuit implementation and microcontroller programming. Mr. Song Hu made a contribution to the data processing, LaTeX editing and proof reading.

Conflicts of Interest

The authors declare no conflict of interest.

References

1. Steigerwald, R.L. A comparison of half-bridge resonant converter topologies. *IEEE Trans. Power Electron.* **1988**, *PE-3*, 174–182.
2. Batarseh, I. Resonant converter topologies with three and four energy storage elements. *IEEE Trans. Power Electron.* **1994**, *9*, 64–73.
3. Bhat, A.K.S.; Dewan, S.B. A generalized approach for the steady state analysis of resonant inverters. *IEEE Trans. Ind. Appl.* **1989**, *25*, 326–338.
4. Li, X.D.; Bhat, A.K.S. Analysis and design of high-frequency isolated dual-bridge series resonant dc/dc converter. *IEEE Trans. Power Electron.* **2010**, *21*, 850–862.
5. Li, X.D.; Li, H.-Y.; Hu, G.-Y.; Xue, Y. A bidirectional dual-bridge high-frequency isolated resonant DC/DC converter. In Proceedings of the 8th IEEE Conference on Industrial Electronics and Applications (ICIEA), Melbourne, Australia, 19–21 June 2013; pp. 49–54.

6. Li, X.D.; Li, H.-Y.; Hu, G.-Y. Modeling of the fixed-frequency resonant LLC DC/DC converter with capacitive output filter. In Proceedings of the 5th IEEE Energy Conversion Congress and Exposition (ECCE), Denver, CO, USA, 15–19 September 2013.
7. Hu, G.-Y.; Li, X.D.; Luan, B.-Y. A generalized approach for the steady-state analysis of dual-bridge resonant converters. *Energies* **2014**, *7*, 7915–7935.
8. Ye, Z.; Jain, P.K.; Sen, P.C. Phasor-domain modeling of resonant inverters for high-frequency AC power distribution systems. *IEEE Trans. Power Electron.* **2009**, *24*, 911–923.
9. Rim, C.T. Unified general phasor transformation for AC converters. *IEEE Trans. Power Electron.* **2011**, *26*, 2465–2475.
10. Batarseh, I.; Siri, K. Generalized approach to the small signal modelling of DC-to-DC resonant converters. *IEEE Trans. Aerosp. Electron. Syst.* **1993**, *29*, 894–909.
11. Agarwal, V.; Bhat, A.K.S. Small signal analysis of the LCC-type parallel resonant converter using discrete time domain modeling. *IEEE Trans. Ind. Electron.* **1995**, *42*, 604–614.
12. Ye, Z.; Jain, P.K.; Sen, P.C. Modeling of high frequency resonant inverter system in phasor domain for fast simulation and control design. In Proceedings of the 39th Annual IEEE Power Elctronics Specialists Conference, Rhodes Island, Greece, 15–19 June 2008; pp. 2090–2096.
13. Sanders, S.R.; Noworolski, J.M; Liu, X.Z.; Verghese, G.C. Generalized averaging method for power conversion circuits. *IEEE Trans. Power Electron.* **1991**, *6*, 251–259.
14. Ye, Z.; Jain, P.K.; Sen, P.C. Multiple frequency modeling of high frequency resonant inverter system. In Proceedings of the 35th Annual IEEE Power Elctronics Specialists Conference, Aache, Germany, 20–25 June 2004; pp. 4107–4113.
15. Agarwal, V.; Bhat, A.K.S. Large signal analysis of the LCC-type parallel resonant converter using discrete time domain modeling. *IEEE Trans. Power Electron.* **1995**, *10*, 222–238.
16. Sosa, J.; Castilla, M.; Miret, J.; de Vicuña, G.L.; Matas, J. Modeling and performance analysis of the dc/dc series-parallel resonant converter operating with discrete self-sustained phase-shift modulation techniques. *IEEE Trans. Ind. Electron.* **2009**, *56*, 697–705.
17. Aboushady, A.A.; Ahmed, K.H.; Finney, S.J.; Williams, B.W. State feedback linearized model for phase-controlled series-parallel resonant converters. In Proceedings of the 37th Annual Conference on IEEE Industrial Electronics Society, Melbourne, Australia, 7–10 November 2011; pp. 1590–1595.
18. Aboushady, A.A.; Ahmed, K.H.; Finney, S.J.; Williams, B.W. Linearized large signal modeling, analysis, and control design of phase-controlled series-parallel resonant converters using state feedback. *IEEE Trans. Power Electron.* **2013**, *28*, 3896–3911.
19. Bhat, A.K.S. Analysis and design of a fixed-frequency LCL-type series-resonant converter with capacitive output filter. *IEE Proc. Circuits Devices Syst.* **1997**, *144*, 97–103.
20. Choi, H.-S. Design consideration of half-bridge LLC resonant converter. *J. Power Electron.* **2007**, *7*, 13–20.
21. Fang, Z.; Cai, T.; Duan, S.; Chen, C. Optimal design methodology for LLC resonant converter in battery charging applications based on time-weighted average efficiency. *IEEE Trans. Power Electron.* **2015**, doi:10.1109/TPEL.2014.2379278.

22. Sarnago, H.; Lucia Gil, O.; Mediano, A.; Burdio, J.M. Analytical model of the half-bridge series resonant inverter for improved power conversion efficiency and performance. *IEEE Trans. Power Electron.* **2015**, doi:10.1109/TPEL.2014.2359576.
23. Buccella, C.; Cecati, C.; Latafat, H.; Pepe, P.; Razi, K. Observer-based control of LLC DC/DC resonant converter using extended describing functions. *IEEE Trans. Power Electron.* **2015**, doi:10.1109/TPEL.2014.2371137.
24. Zheng, R.; Liu, B.; Duan, S. Analysis and parameter optimization of start-up process for LLC resonant converter. *IEEE Trans. Power Electron.* **2015**, doi:10.1109/TPEL.2015.2389116.